Flame Self-Interactions in Turbulent Homogeneous-Mixture n-heptane MILD Combustion

K. Abo-Amsha, N. Chakraborty
School of Engineering, Newcastle University, Newcastle Upon Tyne
NE1 7RU, United Kingdom

1 Introduction

The ever more stringent environmental regulations in response to climate change dictate the need for novel combustion techniques that are simultaneously energy efficient and environmentally friendly. Among such techniques, Moderate or Intense Low-oxygen Dilution (MILD) combustion has been demonstrated to have the potential to achieve both high energy efficiency and ultra-low emissions [1]. A combustion process is considered to be under MILD conditions if the fuel-oxidiser mixture is preheated above its autoignition temperature ($T_r > T_{ign}$), while the maximum temperature rise remains smaller than the autoignition temperature ($\Delta T|_{\max} < T_{ign}$) [1]. Such conditions could potentially be achieved by recirculating exhaust gases (EGR) back to the combustor in furnaces and boilers.

The presence of flame fronts in MILD combustion was shown using Planar Laser-Induced Fluorescence images of OH radicals (OH-PLIF), but indications of distributed burning were revealed through temperature measurements [2]. Minamoto et al. [3] assessed previous experimental findings using Direct Numerical Simulation (DNS) data and indicated that the distributed nature combustion can be attributed to the interaction of thin reaction zones. Thus, the interaction of reaction zones (i.e. flame surfaces) plays a key role in MILD combustion. Moreover, further DNS investigations suggested that modified flamelet-based models can be applied to gaseous fuel MILD combustion [4]. However, when the conventional flamelet and eddy dissipation approaches were applied under MILD conditions in Reynolds Averaged Navier-Stokes (RANS) and Large Eddy Simulations (LES) type studies, they provided good predictions for the mean velocity and temperature fields, but discrepancies with experiments have been reported in terms of peak temperature and minor species concentrations [5, 6]. Thus, further investigations are needed to fully understand the behaviour of flamelet-based approaches in MILD combustion.

When using the flamelet approach, particularly the Flame Surface Density (FSD) equation or the G-equation, the geometry of the flame and the local topology of Flame Self-Interactions (FSI) play an important role. The local topology of FSI influences events such as pocket burnout and cusp formation, which can significantly affect the balance of flame area production and destruction and thus influence the overall burning rate and flame propagation [7]. Different approaches have been used in the literature to characterise the FSI events. These include the critical point theory [7], automatic feature extraction technique using complex wavelet transform [8], and Minkaowski functional based approach [3]. In MILD combustion, Minamoto et al. [3] used Minkowski functionals to study the morphology of the reaction zones in methane-air mixtures, which resulted in a shapefinders map based on planarity and

Correspondence to: khalil.abo-amsha@newcastle.ac.uk

filamentarity parameters for the convenient classification of the reaction zone morphological structures. The reaction zones in MILD combustion showed a variety of shapes including blobs, pancakes and ribbons. However, the pancake-like shapes were found to be the most probable. These shapes are associated with autoignition events and propagating-flames of reactants, products and intermediates mixtures as well as their interactions [3].

The present analysis adopts the critical point theory to investigate the effect of turbulence intensity and dilution level on FSI in turbulent, homogeneous mixture, n-heptane MILD combustion. For this purpose, a DNS dataset of EGR-type, homogeneous-mixture, n-heptane/air MILD combustion cases at two dilution levels ($X_{O_2} = 4.5\%, 3.0\%$) and two turbulent intensities ($u' = 2.0,\ 4.0$ m/s) has been considered.

2 Mathematical Background

For this analysis, the reaction progress variable c has been defined based on the oxidiser mass fraction (Y_{O_2}) as follows:

$$c = \frac{(1-\xi)Y_{O_2,2} - Y_{O_2}}{(1-\xi)Y_{O_2,2} - \max\left[0, \frac{\xi_{st}-\xi}{\xi_{st}}Y_{O_2,2}\right]} \tag{1}$$

where $Y_{O_2,2}$ is the oxidiser mass fraction in the oxidiser stream, while $\xi = (\beta - \beta_2)/(\beta_1 - \beta_2)$ and $\xi_{st} = -\beta_2/(\beta_1 - \beta_2)$ are the mixture fraction and the stoichiometric mixture fraction, respectively [9]. The subscripts 1, 2 refer to the fuel and (diluted) oxidiser streams, respectively. Here $\beta = 2Z_c/W_c + 0.5Z_H/W_H - Z_O/W_O$, Z_j and W_j are the elemental mass fractions and atomic masses for carbon, oxygen and hydrogen atoms. While the critical point theory approach for FSI is rather insensitive to the choice of progress variable species [7] (as long as the resulting c is continuous and monotonic), defining c based on oxygen is justified since larger hydrocarbons, like n-heptane, break done to smaller ones at high temperatures, and thus a fuel based progress variable may not represent the entire combustion process. At the critical points in the flame, the gradient of c goes to zero, and thus a Taylor series expansion around a critical point can be written as:

$$c(\vec{a} + \vec{x}) = c(\vec{a}) + \frac{\vec{x}^T}{2}\underline{\underline{H}}(c(\vec{a}))\vec{x} + \dots \tag{2}$$

where the Hessian $\underline{\underline{H}}(c)$ gives a second order accurate representation of the local field. Since $\underline{\underline{H}}(c)$ is symmetric, its eigenvalues ($\lambda_1,\ \lambda_2,\ \lambda_3$) are real. These eigenvalues describe the curvature along the three principle axes and thus fully characterize (with second order accuracy) the local topology as long as the orientation of structures remains irrelevant [7]. More insights can be obtained by converting the principle axes to spherical coordinates. Following Griffiths et al. [7] and for $\lambda_1 > \lambda_2 > \lambda_3$, the longitude ($\theta$) about the vector $[e_{\lambda_1},\ 0,\ -e_{\lambda_3}]$ is written as:

$$\theta = \frac{6}{\pi}\arctan\left(\frac{(\lambda_1 - 2\lambda_2 + \lambda_3)/\sqrt{6}}{(\lambda_1 - \lambda_3)/\sqrt{2}}\right) \tag{3}$$

while the latitude (φ) about the pole vector $[e_{\lambda_1},\ e_{\lambda_2},\ e_{\lambda_3}]$ is given by:

$$\varphi = \frac{2}{\pi}\arctan\left(\frac{(\lambda_1 + \lambda_2 + \lambda_3)\cos\left(\frac{\theta\pi}{6}\right)/\sqrt{3}}{(\lambda_1 - \lambda_3)/\sqrt{2}}\right) \tag{4}$$

The magnitude of the eigenvalues ($\kappa = \sqrt{\lambda_1^2 + \lambda_2^2 + \lambda_3^2}$) provides an overall curvature measure. Thus, φ and θ are considered as shaping factors which define a continuous domain describing the various

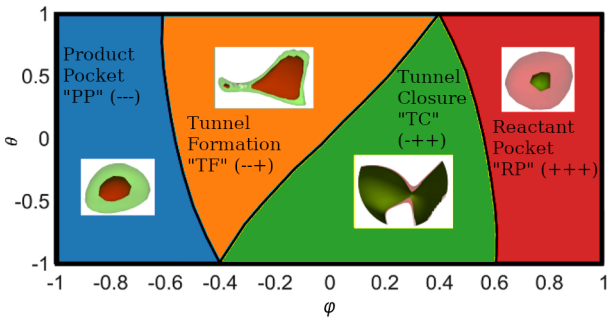

Figure 1: Various types of FSI topologies

feasible local topologies of FSI, as shown in Fig. 1. It can be seen from Fig. 1 that the eigenvalues of the Hessian $\underline{\underline{H}}(c)$ take the signs $(---)$, $(--+)$, $(-++)$ and $(+++)$ from left to right. These signs correspond to Product Pocket (PP), Tunnel Formation (TF), Tunnel Closure (TC) and Reactant Pocket (RP) topologies, respectively. The PP (RP) topologies represent a spherical flame propagating outward (inwards), while the TF and TC topologies correspond to cylindrical flames. In the case of TF topology, the cylindrical flame is propagating away from the common axis, while the opposite is true for TC topology. It is also useful to classify the local flame geometry based on the local mean curvature $\kappa_m = (\kappa_1 + \kappa_2)/2$ and the Gauss curvature $\kappa_g = \kappa_1\kappa_2$, where κ_1, κ_2 are the principle curvatures [10]. Excluding the complex curvature region ($\kappa_g > \kappa_m^2$), positive (negative) value for κ_m suggests that the flame surface is convex (concave) towards the reactant side, while the sign of κ_g indicates the topology type (positive κ_g for an elliptic topology, and negative for a hyperbolic, saddle-like structures).

3 Numerical Implementation

In the current analysis, a DNS dataset of EGR type, turbulent, homogeneous mixture, n-heptane MILD combustion cases at two dilution levels and two turbulent intensities has been considered. For these simulations, the cubic domain ($L = 20\ mm$) has been discretised by a uniformly spaced Cartesian grid comprising of 216 nodes in each direction. This grid resolution ensures that the thermal flame thickness ($\delta_{th} = (T_p - T_r)/\max|\nabla T|_L$ where T, T_p and T_r are the instantaneous, products and reactants temperatures and the subscript L refers to the 1D unstretched laminar flame) has been resolved by a minimum of 15 grid points, while the Kolmogorov length scale (η) has been resolved using 1.1 grid points. Turbulent inflow boundary with specified density, velocity and species mass fractions has been imposed at the inlet boundary, while a partially non-reflective outflow boundary condition has been utilised for the outlet. All other boundaries have been treated as periodic. The process for creating the initial scalar and turbulence fields was described in detail by Minamoto et al. [11]. Table 1 shows the thermochemical and turbulent conditions in the unburned gas. These include the mole fractions of the oxidiser stream, unstretched laminar burning velocity and Zeldovich flame thickness ($\delta_f = \alpha_T/S_L$ where α_T is the thermal diffusivity of the mixture.). The turbulence levels used in this study are comparable to those reported by Oldenhof et al. [12]. The unburned gas temperature of $T_r = 1100$ K is also comparable to that used in the experimental investigation by Ye et al. [13]. The mean inflow velocity U_{mean} was chosen to be 6.0 m/s for all cases. The simulations have been run for two flow-through times (i.e. $\tau_{\text{sim}} = 2.0L/U_{\text{mean}}$), which amounts to 6.67 and 13.34 initial eddy turnover times for the low (HM-A1, HM-B) and high (HM-A2) turbulence cases, respectively.

The simulations in this study have been conducted using the compressible, finite difference DNS code SENGA2. In this code, the dimensional form of the compressible mass, momentum, energy and species

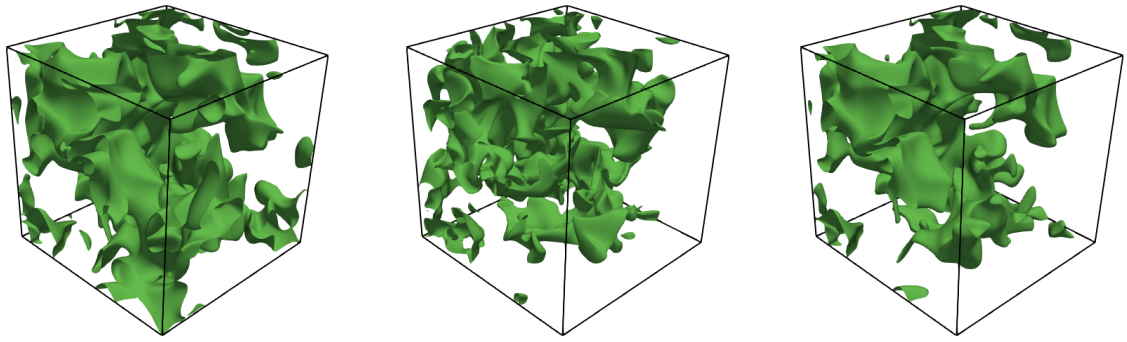

(a) HM-A1 (b) HM-A2 (c) HM-B

Figure 2: The iso-surfaces of c at the location of maximum heat release for the equivalent lamniar flames ($c = 0.71$ for HM-A1, HM-A2 and $c = 0.75$ for HM-B).

mass fractions transport equations are solved with chemical reaction and temperature dependent thermo-physical properties (viscosity, thermal conductivity, specific heat capacities and mass diffusivities). A 10^{th} order central difference scheme is used for spatial discretisation at the internal grid points, which reduces to a one-sided fourth-order accurate scheme at the non-periodic boundaries. For time stepping, a fourth-order explicit low storage Runge-Kutta scheme is used. The boundary conditions are specified according to the Naiver-Stokes Characteristic Boundary Condition (NSCBC) methodology. A reduced chemical mechanism comprising 22 species and 18-steps has been taken to represent the chemical kinetics of combustion [14].

Table 1: Initial conditions for turbulence and scalar fields in n-heptane MILD combustion simulations.

Case	$X_{O_2,2}$	$X_{CO_2,2}$	$X_{H_2O,2}$	ϕ	S_L [m/s]	δ_f [m]	u' [m/s]	ℓ_0 [m]	ℓ_c/ℓ_0
HM-A1	0.045	0.097	0.112	0.8	0.420	4.55×10^{-4}	2.0	2.0×10^{-3}	1.225
HM-A2	0.045	0.097	0.112	0.8	0.420	4.55×10^{-4}	4.0	2.0×10^{-3}	1.225
HM-B	0.030	0.106	0.122	0.8	0.246	7.84×10^{-4}	2.0	2.0×10^{-3}	1.225

4 Results and Discussion

The instantaneous views of c iso-surfaces for all cases are shown in Fig. 2. These c iso-surfaces were constructed at the location of maximum heat release for the equivalent unstretched laminar premixed flame used to initialise each case (Here, $c = 0.71$ for HM-A1, HM-A2 and $c = 0.75$ for HM-B), and thus it can be considered to represent the flame surface. The distributed nature of the flame in MILD combustion, observed in OH-PLIF visualisations by Plessing et al. [2], is evident in Fig. 2. The figure also shows a considerable amount of flame self-interactions at these c iso-surfaces. It can also be seen that increasing the turbulence intensity (case HM-A2) gives rise to a noticeably more wrinkled c iso-surfaces. Comparing Fig.2a and Fig.2c shows that increasing the dilution factor resulted in the c iso-surfaces covering smaller portion of the domain.

The frequency of FSI topologies for different values of c is shown in Fig. 3. For the cases at low turbulence intensity (HM-A1, HM-B), the frequency of FSI events peaks at $c = 0.5$, while the peak frequency is shifted to $c \approx 0.6$ for the case at high turbulence intensity (HM-A2). Fig. 3 also shows that increasing the dilution factor reduces the frequency of FSI events across the entire range of c values. A

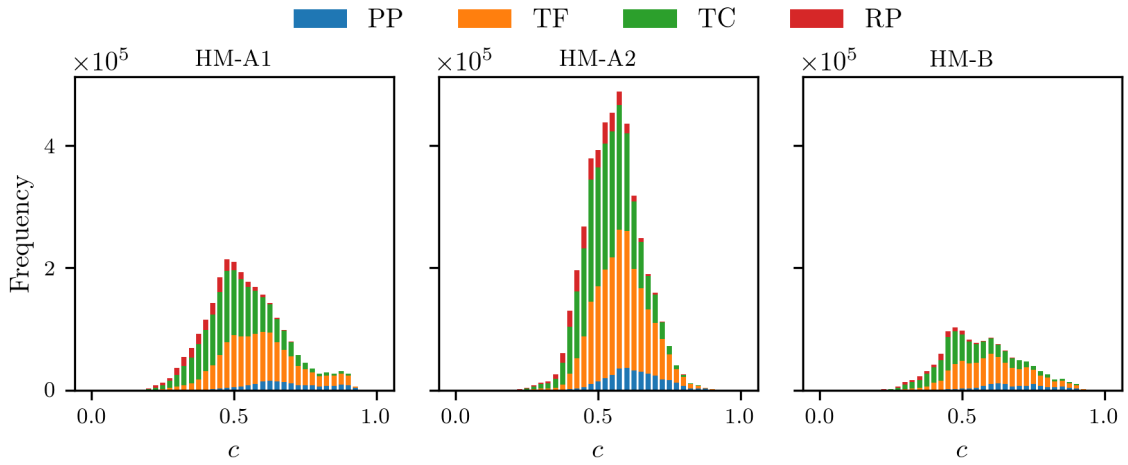

Figure 3: Histogram of the number of samples of the four FSI topologies at different values of c.

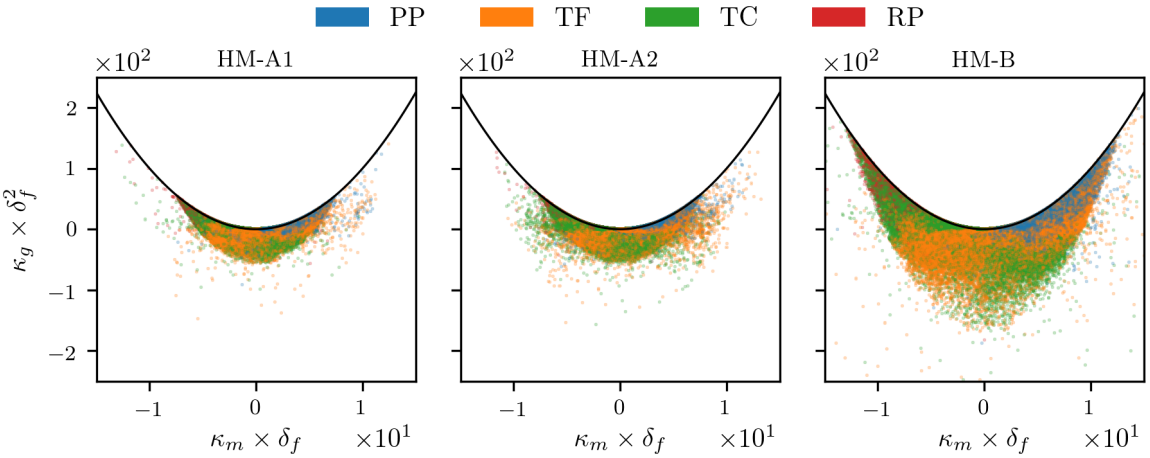

Figure 4: Scatter of $\kappa_g \times \delta_f^2$ with $\kappa_m \times \delta_f$ in the region $0.01 \leq c \leq 0.99$. Scatter is coloured by the different FSI topologies.

possible explanation for this behaviour is that the reduced oxygen concentration makes it more difficult to progress the chemical reaction, and thus reduces the overall sample at high c levels and with it the frequency of FSI events. For all cases, the cylindrical structures (TF and TC) are the most probable FSI events, while the Reactant Pocket (RP) topology is the rarest. This is consistent with the findings reported in the literature [7].

Fig. 4 shows the scatters of FSI events in the $\kappa_m - \kappa_g$ space. It can be seen from Fig. 4 that, in all cases, the PP topology is predominantly associated with elliptic convex structures, while the TF FSI events were most common in the regions representing concave and convex saddle-like structures. As for the TC topologies, both convex saddle-like and elliptic concave structures were common. One can see from Fig. 4 that increasing the turbulence intensity gives rise to a wider spread in FSI topologies along the κ_m axes, while decreasing the oxygen concentration in the mixture resulted in increased levels of the mean and Gauss curvatures for the FSI events. The implications of these FSI events on the modelling of MILD combustion will be discussed in the full paper.

5 Conclusions

The topologies associated with Flame Self-Interaction (FSI) events were investigated using the critical point theory for turbulent, homogeneous mixture n-heptane/air MILD combustion. The local flame geometry has also been categorised using the mean and Gauss curvatures. The peak frequencies of FSI events were found to be in the range $c = 0.5 - 0.6$. It was found that increasing the turbulence intensity has led to enhanced FSI frequency and resulted in higher mean curvature levels. This is consistent with experience, since higher turbulence intensities lead to stronger flame wrinkling. Increasing the dilution factor caused a reduction in the frequency of FSI events towards the burned gas side, but produced higher levels of mean and Gauss curvatures.

Acknowledgement

The authors are grateful to EPSRC (EP/S025154/1) for the financial support. The computational support was provided by ARCHER2 (EP/R029369/1) and the HPC facility at Newcastle University (Rocket).

References

[1] A. Cavaliere and M. de Joannon. Mild Combustion. *Progress in Energy and Combustion Science*, 30(4):329–366, January 2004.

[2] T. Plessing, N. Peters, and J. G. Wünning. Laseroptical investigation of highly preheated combustion with strong exhaust gas recirculation. *Symposium (International) on Combustion*, 27(2):3197–3204, January 1998.

[3] Y. Minamoto, N. Swaminathan, R. S. Cant, and T. Leung. Morphological and statistical features of reaction zones in MILD and premixed combustion. *Combustion and Flame*, 161(11):2801–2814, November 2014.

[4] Y. Minamoto and N. Swaminathan. Subgrid scale modelling for MILD combustion. *Proceedings of the Combustion Institute*, 35(3):3529–3536, January 2015.

[5] J. Aminian, C. Galletti, S. Shahhosseini, and L. Tognotti. Key modeling issues in prediction of minor species in diluted-preheated combustion conditions. *Applied Thermal Engineering*, 31(16):3287–3300, November 2011.

[6] F. C. Christo and B. B. Dally. Modeling turbulent reacting jets issuing into a hot and diluted coflow. *Combustion and Flame*, 142(1):117–129, July 2005.

[7] R. A. C. Griffiths, J. H. Chen, H. Kolla, R. S. Cant, and W. Kollmann. Three-dimensional topology of turbulent premixed flame interaction. *Proceedings of the Combustion Institute*, 35(2):1341–1348, January 2015. ISSN 1540-7489.

[8] T. D. Dunstan, N. Swaminathan, K. N. C. Bray, and N. G. Kingsbury. Flame Interactions in Turbulent Premixed Twin V-Flames. *Combustion Science and Technology*, 185(1):134–159, January 2013.

[9] R. W. Bilger. The structure of turbulent nonpremixed flames. *Symposium (International) on Combustion*, 22(1):475–488, January 1989.

[10] C. Dopazo, J. Martín, and J. Hierro. Local geometry of isoscalar surfaces. *Physical Review E*, 76(5):056316, November 2007.

[11] Y. Minamoto, T. D. Dunstan, N. Swaminathan, and R. S. Cant. DNS of EGR-type turbulent flame in MILD condition. *Proceedings of the Combustion Institute*, 34(2):3231–3238, January 2013.

[12] E. Oldenhof, M. J. Tummers, E. H. van Veen, and D. J. E. M. Roekaerts. Role of entrainment in the stabilisation of jet-in-hot-coflow flames. *Combustion and Flame*, 158(8):1553–1563, August 2011.

[13] J. Ye, P. R. Medwell, M. J. Evans, and B. B. Dally. Characteristics of turbulent n-heptane jet flames in a hot and diluted coflow. *Combustion and Flame*, 183:330–342, September 2017.

[14] S. Liu, J. C. Hewson, J. H. Chen, and H. Pitsch. Effects of strain rate on high-pressure nonpremixed n-heptane autoignition in counterflow. *Combustion and Flame*, 137(3):320–339, May 2004.